





Ultra Wideband Dual-Output Thin Film Lithium Niobate Intensity Modulator

Xiaofeng Zhu , Marco Moller de Freitas , Shouyuan Shi , *Member, IEEE*, Andrew Mercante, Peng Yao, Fuquan Wang, Benjamin A. Shopp, Christopher J. Cullen, and Dennis W. Prather , *Fellow, IEEE*

(Invited Paper)

Abstract—This paper presents the design, optimization, fabrication, and characterization of a dual-output, wideband, thin-film lithium niobate Mach-Zehnder Modulator (TFLN-MZM). The device is designed with ridge etched waveguides for operation at a $1.55 \mu\text{m}$ wavelength. The dual-output is achieved using a 2×2 multi-mode interference (MMI) splitter with an extinction ratio (ER) of over 40 dB. The measured DC half-wave voltage (V_π) is 1.02 V. To achieve wideband operation, segmented electrodes are optimized to provide both wideband index matching and low loss. Accordingly, the measured 3 dB bandwidth is 95 GHz and the radio-frequency (RF) electrode loss is $0.24 \text{ dB}/(\text{cm} \cdot \text{GHz}^{1/2})$. The motivation for this device is in balanced microwave photonic links (MPLs) for Radio-Frequency-over-Fiber (RFoF) applications.

Index Terms—LNOI, dual-output MZM, microwave photonic link.

I. INTRODUCTION

WITH mobile communications and wireless networks advancing from 5th to 6th generation (5G to 6G), RF frequencies are rapidly migrating up into the millimeter wave (mmW) region of the electromagnetic spectrum. However, at these frequencies, the losses in simple cables and waveguides becomes significant, which is giving rise to a renewed interest in RFoF links [1], or MPLs [2]. In this approach, an input RF/mmW signal is up-converted to the optical domain via an electro-optic modulator (EOM), input to an optical fiber for transport with low loss ($\approx 0.2 \text{ dB}/\text{km}$), and at the other side of the link the RF signal is recovered using a photodetector (PD). The key performance parameters for such a link are low noise-figure (NF), high RF gain, and high spur-free-dynamic-range (SFDR). Each of these parameters depend on an efficient up-conversion of

Manuscript received 28 November 2023; revised 16 March 2024; accepted 7 April 2024. Date of publication 12 April 2024; date of current version 19 April 2024. This work was supported in part by the Air Force Office of Scientific Research (AFOSR) under Grant FA9550-20-1-0301, and in part by the Office of Naval Research (ONR) under Grant N00014-21-1-2263. (Corresponding author: Xiaofeng Zhu.)

Xiaofeng Zhu, Marco Moller de Freitas, Shouyuan Shi, Christopher J. Cullen, and Dennis W. Prather are with the Electrical and Computer Engineering Department, University of Delaware, Newark, DE 19716 USA (e-mail: xzhu@udel.edu).

Andrew Mercante, Peng Yao, Fuquan Wang, and Benjamin A. Shopp are with the Phase Sensitive Innovations, Inc., Newark, DE 19713 USA.

Color versions of one or more figures in this article are available at <https://doi.org/10.1109/JSTQE.2024.3388324>.

Digital Object Identifier 10.1109/JSTQE.2024.3388324

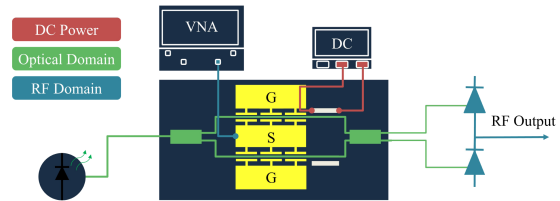


Fig. 1. Intensity modulation direct detection (IMDD) link by using dual-output TFLN-MZM.

the RF/mmW signal to the optical domain by the EOM and high photocurrent generation by the PD. In this case, the efficiency of the EOM is governed by its V_π (the lower the better) and the photocurrent from the PD is governed by its responsivity (A/W) (the higher the better).

Even though advanced devices have been made in terms of EOMs with low V_π 's, i.e., less than 1 V [3] and PDs with photocurrents on the order of 10's to 100 mA [4], the overall performance of MPLs still suffered from the relative intensity noise (RIN) imposed by the laser. For this reason, intensity-modulated-direct-detection (IMDD) links had unacceptably high noise-figure (NF), low RF gain, and modest spur-free-dynamic-range (SFDR). To address these limitations, balanced links have been developed and shown to mitigate RIN to the point where shot noise limited performance can be achieved [2]. In this case, one can continually improve the NF and RF gain of the link so long as the balanced-PD (BPD) can produce sufficiently high photocurrents. Assuming this can be achieved, the BPD must have a common-mode-rejection-ratio (CMRR) of $>20 \text{ dB}$ and the EOM must be a dual-output modulator with an extinction ratio between the dual-outputs of $>20 \text{ dB}$. This being the case, another significant advantage of a balanced link is an inherent increase in RF gain of 6 dB, which results from having a 3 dB increase in photocurrent due to the current produced from each of the dual outputs. The dual-output TFLN-MZM reported in this paper has an extinction ratio (ER) $>40 \text{ dB}$ between the dual-outputs, while also improving the other device performance parameters such as V_π and bandwidth. Having such a high ER enables the use of this modulator design in association with balanced photodetectors to form a balanced RF over fiber (RFoF) link, as shown below in Fig. 1.

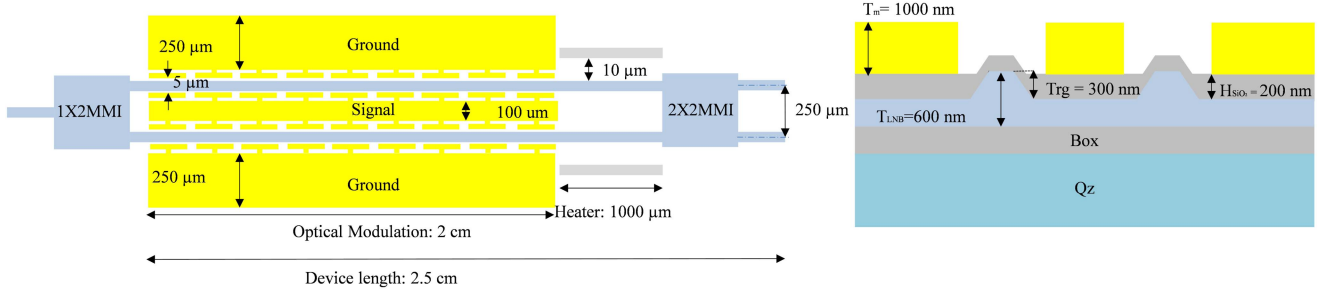


Fig. 2. Fig 1. (a) Layout of the designed dual-output TFLN MZM. (b) The Cross-section view of the dual output MZM, parameters $(W_{gap}, W_{sig}, W_{rg}, H_m, H_{rg}, H_{LNB}, H_{box}) = (5, 100, 1, 0.3, 0.6, 2) \mu\text{m}$.

In the design of dual-output EOMs, a wide operational bandwidth is also desirable in order to accommodate the ever-increasing range of wireless network frequencies. However, typically, there is a trade-off between simultaneously achieving a low V_π and ultra-wideband operation. This work has overcome this trade-off by developing and optimizing index-matched slow wave electrodes. In the next section, the details of the device design and simulation are presented.

II. DEVICE DESIGN AND SIMULATION

During the last decade, thin-film lithium niobate has emerged as a material of significant interest owing to its superior optical properties, such as broad transparency window, high second-order nonlinearity ($r_{33}=31.8 \text{ pm/V}$) and a low third-order nonlinearity. In addition, it is notable that TFLN-MZMs have been shown to operate with high optical powers, i.e., $>2 \text{ W}$, as well as significantly higher modulation speeds in comparison to other materials such as silicon [5] and Indium Phosphide (InP) [6]. Historically, bulk lithium niobate modulators suffer from a relatively high $V_\pi \cdot L$ and limited operational bandwidth. However, with the advent of smart cut thin-film lithium niobate on insulator (TFLNOI), the optical mode size has been significantly reduced thereby enabling the electrode gap to be narrowed down to just a couple micrometers, which lowers the $V_\pi \cdot L$. The tradeoff, however, between simultaneously achieving a low V_π and high 3 dB bandwidth remained a challenge until the introduction of segmented electrodes [7]. In this work, a similar approach has been used for a dual-output modulator, which is presented below. Although dual-output modulators have been demonstrated on silicon [8] and InP [9] material platforms, they have only been demonstrated with a 3 dB bandwidth of 26 and 28 GHz, respectively, due mainly to their inherent material properties.

In this work, High-Frequency-Structure-Simulator (HFSS) is used to perform a comprehensive analysis and optimization of both the RF electrodes and the TFLN-MZM device performance. In particular, to realize improved electro-optic modulation at high frequencies and to optimize RF and optical mode confinement and overlap, we focused on optimizing the electrode gap and the underlying silicon dioxide (SiO_2) buffer layer thickness. To ensure index matching between the optical group index and the RF phase index, segmented electrodes were used to tune the RF phase effective index. Thus, by modifying the electrode's

structure, index matching between the RF phase index and optical group index was achieved to the second decimal place for a 20 mm long device up to 110 GHz operation. The end result was a dual-output TFLN-MZM with a V_π of 1.02 V and 3 dB bandwidth of 95 GHz, which were experimentally demonstrated. The layout for this device is shown in Fig. 2(a), which consists of optical waveguides (gray), being driven by high-frequency segmented electrodes (yellow). A thermo-optic phase shifter is used to establish a DC bias condition and the two parallel optical waveguides are driven by RF electrodes operated in a push-pull configuration. The output from each waveguide is input to a 2×2 MMI that produces two outputs from the modulator, or a dual-output.

The segmented electrode is used to slow the RF signal, so the RF phase index in order to match it to the optical group index to within ± 0.01 , which enables wide band operation. A thermo-optic phase shifter is used to provide a DC bias in one arm of the MMI to achieve quadrature bias for optimal linear response. In the modulator design, the mode overlap of the optical mode within the TFLN waveguide and the electric field directly influence the modulation performance of the entire device. Since the mode overlap is affected by the electrical gap and buffer, a trade-off study was performed to optimize the performance of the modulator design. Additionally, 1×2 and 2×2 MMI splitters are employed for signal splitting and recombination. As such, a comprehensive simulation and optimization process was performed to reduce MMI loss and minimize unbalanced power splitting. Lastly, segmented electrode design was performed to minimize electrode losses while achieving a 50Ω impedance match as well as index matching.

A. Electrical-Optic Trade-Off Studying

In most modulators, such as phase modulators [10], MZM [3], Michelson Interferometer modulators [11], and others, one of the most important parameters is the V_π , which is dependent on the group index of the optical waveguide mode, the operational wavelength, the gap between the electrodes, the RF mode that overlaps with the optical waveguide, and the overall length of the device. The DC- $V_\pi \cdot L$ can be expressed as the following equation:

$$V_\pi \cdot L = \frac{\lambda_0 d}{n_e^3 r_{33} \Gamma_{mode}} \quad (1)$$

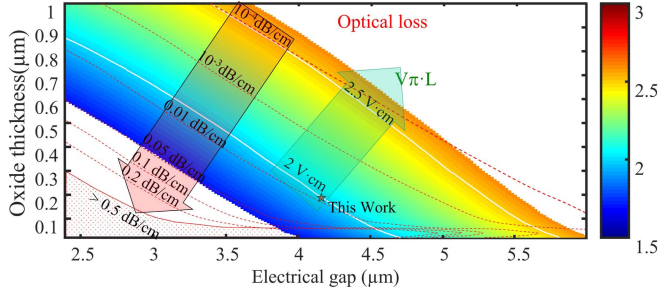


Fig. 3. Simulation study results of thickness of cladding SiO_2 layer, electrode gap, $V_\pi \cdot L$, and the induced optical loss due to metal absorption.

where V_π represents the half-wave voltage, λ_0 is the wavelength, n_e denotes the effective index, r_{33} represents the Pockels coefficient, and Γ_{mode} is the electrical field and optical mode overlap ratio. In (1), the electric field and optical mode are not fully overlapped. For a ridge-etched lithium niobate modulator, the mode overlapping can be written as:

$$\Gamma_{mode} = \frac{\int \int_{LN} \frac{1}{2} n_e^3 r_{33}(x, z) E_m(x, z) |E_o(x, z)|^2 dx dz}{V_0 \int |E_o(x, z)|^2 dx dz} \quad (2)$$

where V_0 is the applied voltage to the electrode, $E_m(x, z)$ is the electrical field as shown in Fig. 9(c). In this design, the optical waveguide is aligned in the Y direction and the electrical field is perpendicular to the optical waveguide in the X and Z directions. In any TFLN-MZM, a longer electrode implies a greater modulation region, thereby requiring a lower voltage to achieve phase modulation. However, longer electrodes can increase the RF loss, thus leading to a reduction in the 3 dB bandwidth. In essence, there is a trade-off relationship between V_π and 3 dB bandwidth. To overcome this relationship, a study was conducted using full-wave electromagnetic simulations in HFSS on the RF mode profile and using Lumerical Mode simulations for the optical waveguide mode, to ensure optimal overlap. In addition, the simulations also focused on minimizing the electrode gap and the optimal thickness of the underlying SiO_2 layer between the optical waveguide and RF electrode. To determine the optical mode, the 70° angle of the lithium niobate ridge-etched waveguide was simulated using Lumerical MODE solver where single mode operation was achieved for a ridge-etched optical waveguide with a ridge width of $1 \mu\text{m}$ and an etch depth of 300 nm on a 600 nm thick TFLN with a $2 \mu\text{m}$ buried oxide (BOX) layer on a Quartz (Qz) handle. The simulated optical waveguide has a mode confinement factor of 89% in the TFLN layer. To meet the requirement of sub-volt V_π an interaction region exceeding several centimeters is necessary, assuming a small electrode gap. However, a narrow gap between the electrodes can interact with the optical mode and introduce loss. To overcome this issue, a SiO_2 buffer layer is introduced between the TFLN layer and the electrodes, which helps to reduce metal absorption loss. As shown in Fig. 3, the red arrow shows that optical loss increases as the thickness of the buffer or the electrical gap is reduced. However, the buffer layer affects the electric field profile that passes through it. Accordingly, an excessively thick oxide layer would place the waveguide too far from the electric field, thereby diminishing the efficiency

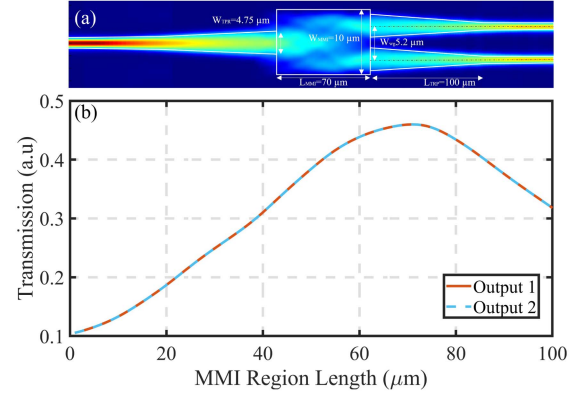


Fig. 4. (a) Top-down view of the mode field plot of 1×2 MMI with all dimensions labeled. (b) Simulated transmission as a function of the length of MMI region for two ports of 1×2 MMI.

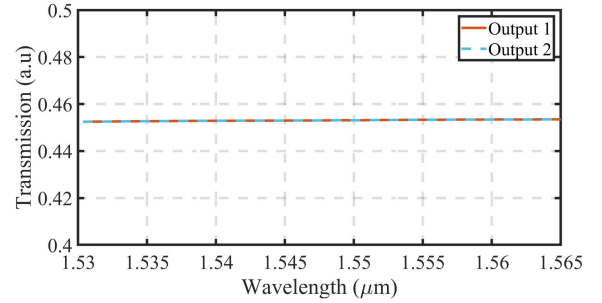


Fig. 5. Simulated transmission as a function of wavelength for two ports of 1×2 MMI.

of electro-optic modulation. The green arrow, in Fig. 3, shows the simulated $V_\pi \cdot L$, which increases as the thickness of the buffer or the electrode gap increases. To optimize the device's performance, a smaller gap can be chosen, however, this can pose challenges for the electron-beam-lithography (EBL) alignment tolerance. For electrodes 20 mm long, larger currents in the range of 100 to 200 nA are often used in the Raith 100 KV EBPG 5200 system to reduce exposure time, which can introduce greater alignment deviations. The marked points in the figure represent the structural designs studied in this experiment and because the electrodes are fabricated using a bi-layer lift-off method, the edges of the electrodes are not entirely perpendicular to the sample surface. This inclination results in a reduction in the electrode gap from the originally designed $5 \mu\text{m}$ to $4.2 \mu\text{m}$, as shown in Fig. 3. The simulation results indicate that the $V_\pi \cdot L$ for this device is around $2 \text{ V} \cdot \text{cm}$, which is near perfectly align with the experimental data.

B. 1×2 Splitter Design

As shown in Fig. 2, a 1×2 MMI splitter was used as a 3 dB splitter before the modulation region. Compared to bidirectional couplers and Y-branches, a 1×2 MMI exhibits a relatively larger physical footprint. However, it offers enhanced performance stability over broadband operation, as shown in Fig. 5. In addition, MMI's are more accommodating to lithography errors that may arise during EBL writing and the subsequent etching processes. To this end, the overall modulator design spans approximately

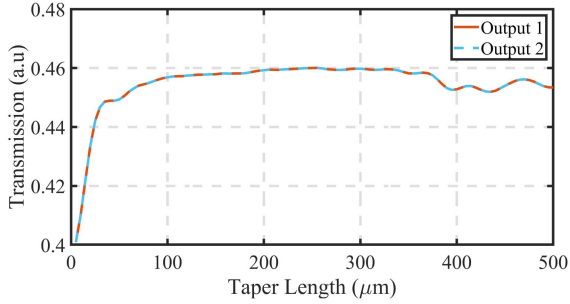


Fig. 6. Simulated transmission as a function of taper length for two ports of 1×2 MMI.

2.5 cm in length wherein deviations on the order of several hundred micrometers have a limited impact on the overall device size. The symmetrical structure of 1×2 MMI further ensures better maintenance of a 50:50 power splitting ratio. To accelerate the simulation process, the length and width of the multimode region are initially estimated using (3):

$$L_{\text{MMI}} = \frac{4n_e w_m^2}{N\lambda_0} \quad (3)$$

where n_e is the effective index of the multimode region, w_e is the width of the multimode region, N is the number of self-images, and λ_0 is the wavelength, shown in Fig. 4(a), (b). In this design, a $70 \mu\text{m}$ length and $10 \mu\text{m}$ width of the multimode region were simulated using Lumerical Mode and FDTD solvers to ensure optimal transmission for both ports. A single-mode waveguide was used to couple light into the multimode region and, for better mode matching, a $4.75 \mu\text{m}$ wide taper was utilized to transition the $1 \mu\text{m}$ wide single-mode coupling into the multimode region. As shown in Fig. 6, the coupling loss was minimized by extending the taper length to $100 \mu\text{m}$. Simulations for the transmission balance for the two output ports is shown in Fig. 5 and the transmission as a function of taper length for the two output ports is shown in Fig. 6.

C. 2×2 Splitter Design

A similar taper design was used for the 2×2 MMI simulation, as shown in Fig. 7(a), (b), where a $286 \mu\text{m}$ length multi-mode region was simulated to have an equal splitting ratio and optimal transmission for the two ports. The splitting ratio of the 2×2 MMI is wavelength dependent and, as such, a transmission simulation was performed from 1530 nm to 1565 nm , where equal splitting occurred at around 1553 nm . Notably, at 1550 nm there is less than 0.05% difference. As shown in Fig. 8, the same taper design has been used to reduce the coupling loss from the single mode to multimode region.

III. SEGMENTED TRAVELING WAVE ELECTRODE DESIGN AND SIMULATION

The segmented electrode simulation was performed using HFSS, which was used to predict the design impact on the RF phase index. In these simulations a fine meshing is critical for accuracy, given the dimensions of the electrodes are relatively small compared to the operational frequency. Thus, to locally

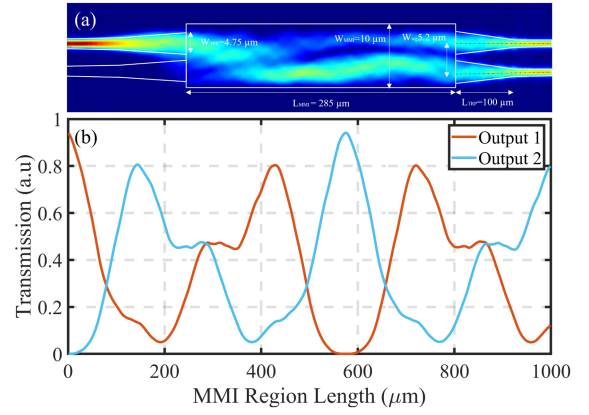


Fig. 7. (a) Top-down view of mode field plot of 2×2 MMI with all dimensions labeled. (b) Simulated transmission as a function of the length of MMI region for two ports of 2×2 MMI.

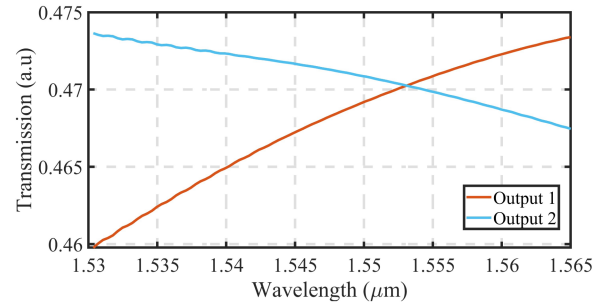


Fig. 8. Transmission of port 1 and 2 as function of wavelength from 1530 nm to 1565 nm .

improve the mesh around the T-rails, all structures around them, including the SiO_2 buffer, Qz handle wafer, and air gap, were divided into blocks, as shown in Fig. 9(b). In this case, different length-based mesh sizes were applied to different blocks based on the feature size each contained. Fig 9(a) shows the parameters that may affect the RF index and electrode losses. They have been labeled as s, g, G, p, d, w, and h, corresponding to signal width, electrode gap, the width of ground, period, duty cycle, T-rail width, and height, respectively. Separate simulation analyses were conducted for each of these parameters. In this study, parameter extraction algorithms were developed in MATLAB based on the transmission line theory. Since the cross-section of the segmented electrode is periodically changing along the CPW and the periodicity is much smaller than the operational wavelength, each period of the T-rail can be considered as a lumped element, which enables an equivalent transmission line model to be developed [12]. The characterization algorithm was then used to characterize the fabricated segmented electrodes by measuring the S-parameters.

As previously discussed, optimizing the thickness of the buffer layer and the distance between the waveguide and electrodes can enhance $V_\pi \cdot L$, which we have optimized with the goal of achieving a DC V_π of 1 V . However, this does not consider the RF losses induced by the electrodes. Thus, in the absence of considerations for radiation loss due to ultra-high frequencies, the sources of electrode losses primarily include material loss,

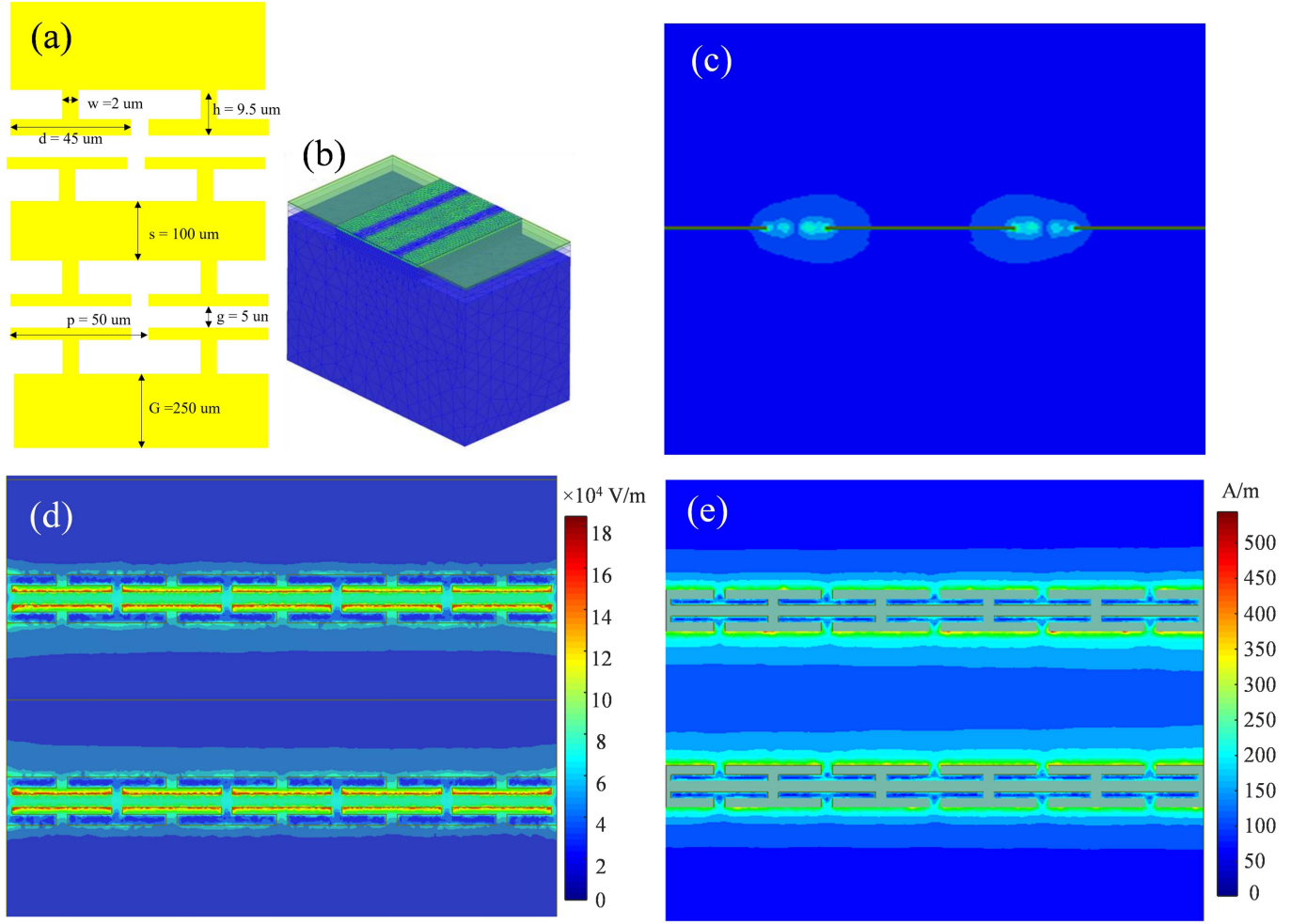


Fig. 9. (a) Layout of the index match segmented electrode design, parameter $(w,h,d,s,p,g,G)=(2,9.5,45,100,50,5,250)\mu\text{m}$. (b) Overview of optimized mesh condition for segmented electrode. (c) Cross-section of electrical field distribution around coplanar waveguide (CPW) overlaps with the optical TFLN waveguide while appended 1 V RF signal. (d) Top-down view of the electrical field along in the TFLN under the segmented electrode, the majority of the field is around the edge of the T-rail as expected. (e) Top-down view of the current distribution, all the current flows along the edge of the CPW not the T-rail.

electrode design issues, and the impact of skin depth. To mitigate material loss and the effect of skin depth, a $1\ \mu\text{m}$ evaporated gold was used as an electrode. Unlike most substrate material choices that favor silicon because of its mature and cost-effective processing, silicon exhibits a significantly high dielectric RF loss, which is not favorable for a segmented electrode design. Therefore, this work uses a Qz substrate that offers an alternative with much lower dielectric RF loss compared to silicon, thereby significantly reducing the material losses. Another critical factor is phase matching, where a good phase index can enhance the modulation depth for high frequency, as shown in (4) and (5).

$$M(f) = 20\lg \left\{ e^{-\frac{\alpha L}{2}} \left[\frac{\sinh^2\left(\frac{\alpha L}{2}\right) + \sin^2\left(\frac{\beta L}{2}\right)}{\left(\frac{\alpha L}{2}\right)^2 + \left(\frac{\beta L}{2}\right)^2} \right]^{\frac{1}{2}} \right\} \quad (4)$$

where $M(f)$ is the modulation depth. α is the loss per unit length of the electrode, L is the length of the electrical optic mode interaction region, and β can be expressed as the following

equation:

$$\beta = (n_\mu - n_0) \frac{2\pi f}{c} \quad (5)$$

where n_μ is the RF phase index n_0 is the optical group index, c is the speed of light, and f is the frequency. In this context, the segmented electrode has been used instead of a conventional CPW, which exhibits a much larger RF phase index and higher losses [13].

As shown in Fig. 9(d), a strong electrical field is concentrated at the edge of the T-rail and, using HFSS, the influence of various parameters on index loss and impedance has been studied. That said, based on a review of the existing literature [14] the periodicity of T-rails below 300 GHz does not significantly affect electrode loss. In addition, a larger signal width helps to reduce electrode loss by having better RF mode matching, however, the losses reach a minimum at around $100\ \mu\text{m}$. Further changing of the width of the signal will increase the capacitance of the electrode, which will also increase the phase index. This being said, a parameter that can be used to tune the RF phase index without affecting electrode losses is preferred. Thus, after

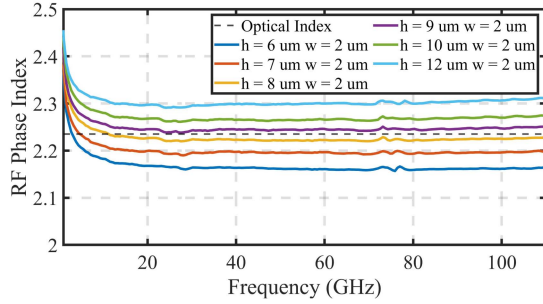


Fig. 10. Measured RF phase index from 500 MHz to 110 GHz with fixed $w = 6 \mu\text{m}$ and sweep h from 6 to 12 μm .

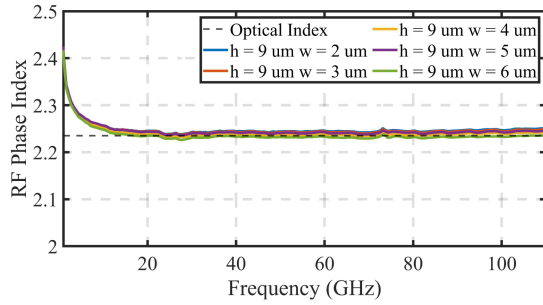


Fig. 11. Measured RF phase index from 500 MHz to 110 GHz with fixed $h = 9 \mu\text{m}$ and sweep w from 2 to 6 μm .

excluding signal width (s), period, and duty cycle (p,d), the T-rail width (w) and height (h) have been found to have a significant impact on the RF phase index and do not introduce additional losses. Therefore, building on this insight, the size of w was varied from 2 μm to 6 μm and h from 6 μm to 12 μm for 10 mm long segmented electrodes, which were fabricated and characterized. They were fabricated on a 600 nm thick TFLN that was etched to a depth of 288 nm using the same etching process developed for low-loss LN waveguide etching. The etching depth was measured to be 312 nm. Additionally, 186 nm PECVD SiO_2 was deposited along with a witness sample. Subsequently, the witness sample was used during the PECVD process to measure the thickness and refractive index of SiO_2 . The refractive index of lithium niobate was provided by NanoLN. Based on the measured refractive index, the optical group index of 2.235 was simulated using Lumerical MODE solver. This sample was used to pattern segmented electrodes following the standard bi-layer lift-off process, as shown in Fig. 15(a). A 700 nm layer of evaporated gold was deposited and soaked in NMP with an 80 $^\circ\text{C}$ water bath for 20 minutes for the lift-off process. In total, 30 samples were fabricated with control variables. As shown in Fig. 10, the RF phase index was measured from 500 MHz to 110 GHz. The results show that the RF phase index can be tuned from 2.13 to 2.30, while sweeping h from 6 μm to 12 μm which serves to further confirm the positive role of segmented electrodes in index tuning.

As shown in Fig. 11, the same measurements were carried out while sweeping w . In this case, the RF phase index can be fine-tuned and matched to nearly the third decimal place. A corresponding colormap is shown in Fig. 12, which summarizes the results of the collective 30 devices. This shows that the RF

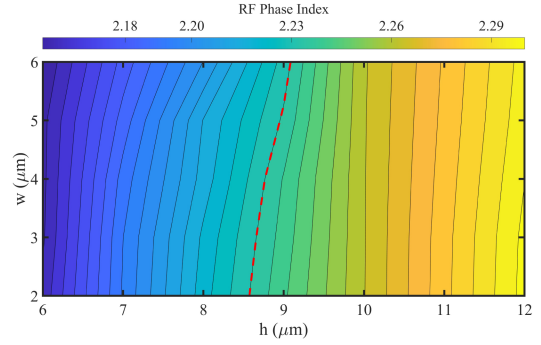


Fig. 12. Heat map of RF index was plotted based on h length change from 6 to 12 μm and w with a sweep from 2 to 6 μm , the red line indicates the simulated optical index 2.235.

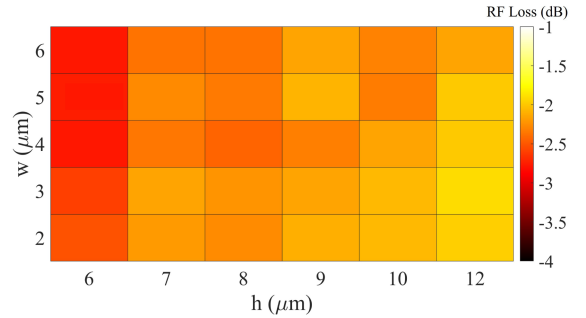


Fig. 13. Heat map of RF loss at 50 GHz was plotted based on h length change from 6 to 12 μm and w with a sweep from 2 to 6 μm .

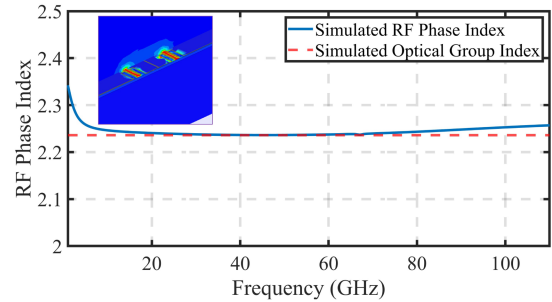


Fig. 14. Simulated RF phase index as function of frequency for 1 mm long segmented electrode.

phase index can be accurately tuned to the third decimal place within a range from 2.13 to 2.30.

In the interim, the RF loss at 50 GHz was calculated for the 10 mm fabricated segmented electrode represented in the form of a heatmap, as shown in Fig. 13. When altering the parameter h , it was observed that the RF loss exhibited an approximate variation of 0.5 dB. Furthermore, an increase in h from 6 μm to 12 μm was noted to correlate with a decreased level of loss. Upon conducting a sweep of the parameter w within the range of 2 μm to 6 μm , it was observed that the loss did not exhibit significant fluctuations, suggesting that this loss may be attributed to the fabrication process. These measured results align with our HFSS simulations, which indicate minimal current flow along the T-rail and the majority of current concentration along the edge of the CPW, as shown in Fig. 9(e). This change of h and w not only contributes to index matching but is also shown to have minimal effect on additional RF losses.

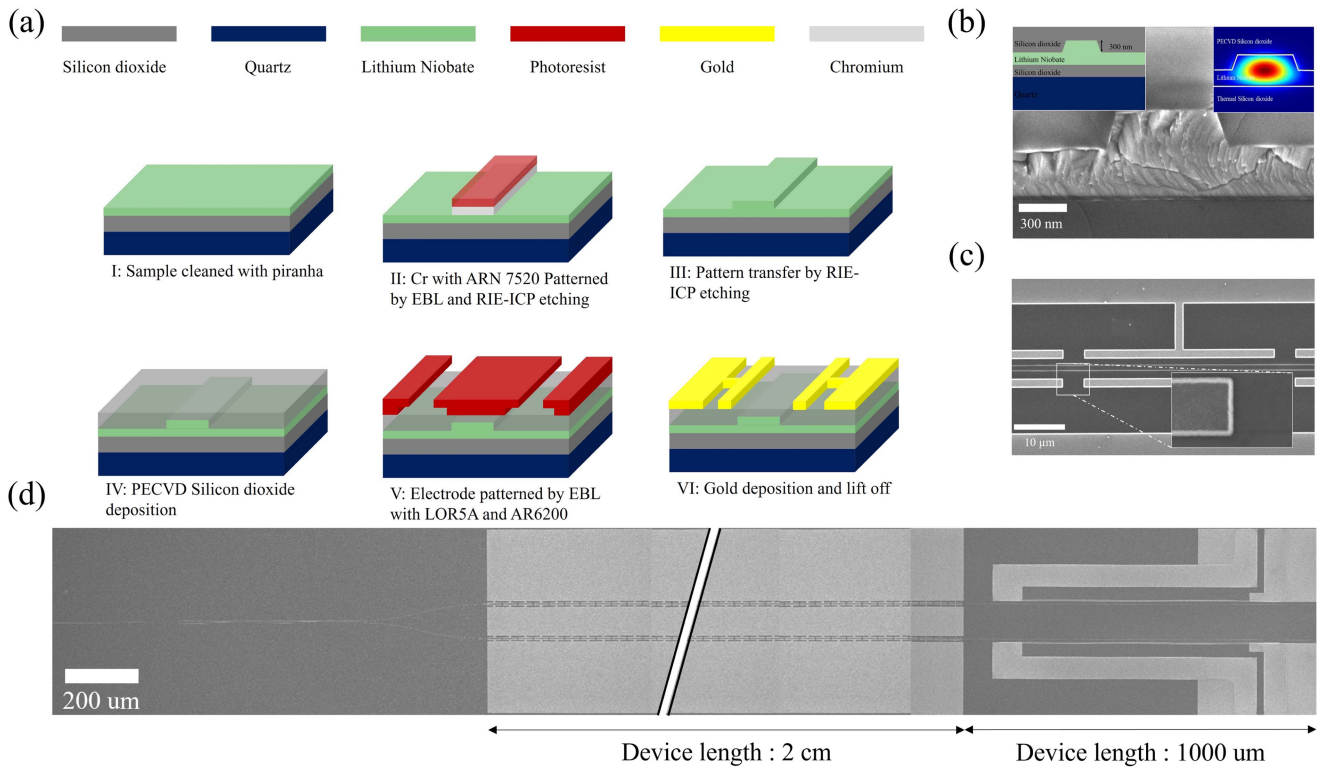


Fig. 15. (a) Overall view of the fabricated segmented electrode. (b) Cross-section of the waveguide and simulated optical mode. (c) SEM pictures of the fabricated TFLN waveguide aligns with the segmented electrode. (d) SEM pictures of the dual output TFLN MZM fabricated.

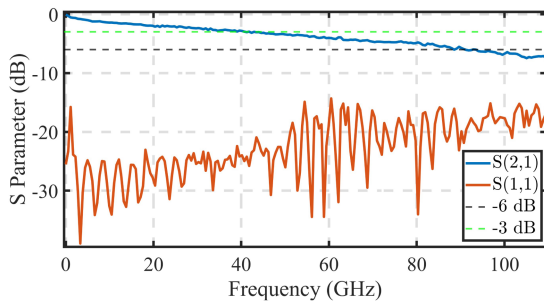


Fig. 16. S_{21} and S_{11} of fabricated 20 mm long segmented electrode from 500 MHz to 110 GHz.

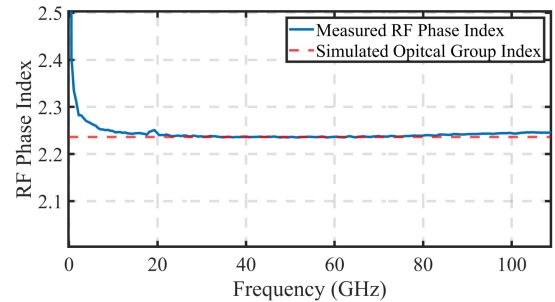


Fig. 18. Calculated RF phase index based on the measured S-parameter from 500 MHz to 110 GHz and simulated optical group index.

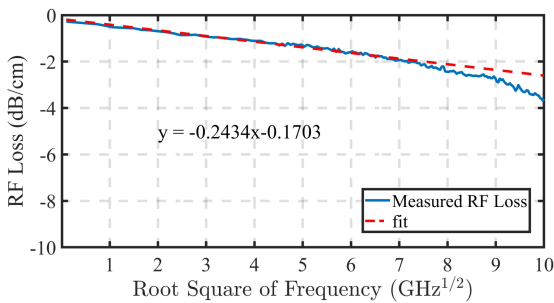


Fig. 17. RF loss for unit length as a function of the square root of the frequency and a linear fit of the electrode loss.

Following these results, the HFSS model was recalibrated using both fabricated and calculated values. The recalibration was necessary because different fabrication methods resulted

in varying relative permittivity values for each material. In this device, the thickness of the Qz handle significantly exceeds that of other materials, causing a modified relative permittivity of Qz, which has a huge impact on the RF phase index. In Fig. 14, the calibrated model was used to design a segmented electrode that exhibited good index matching from 1 GHz to 110 GHz. The figure also displays a field plot of the 1 mm long unit cell of the segmented electrode. Based on this simulated design, the dual-output TFLN-MZM is then processed based on the optimization of the optical and RF domains.

IV. FABRICATION

As shown in Fig. 15(a), the 600 nm thick X-cut TFLN from NanoLN was cleaned by using $H_2SO_4:H_2O_2(3:1)$ for 1 min followed by DI rinse for 5 min. Alignment makers were

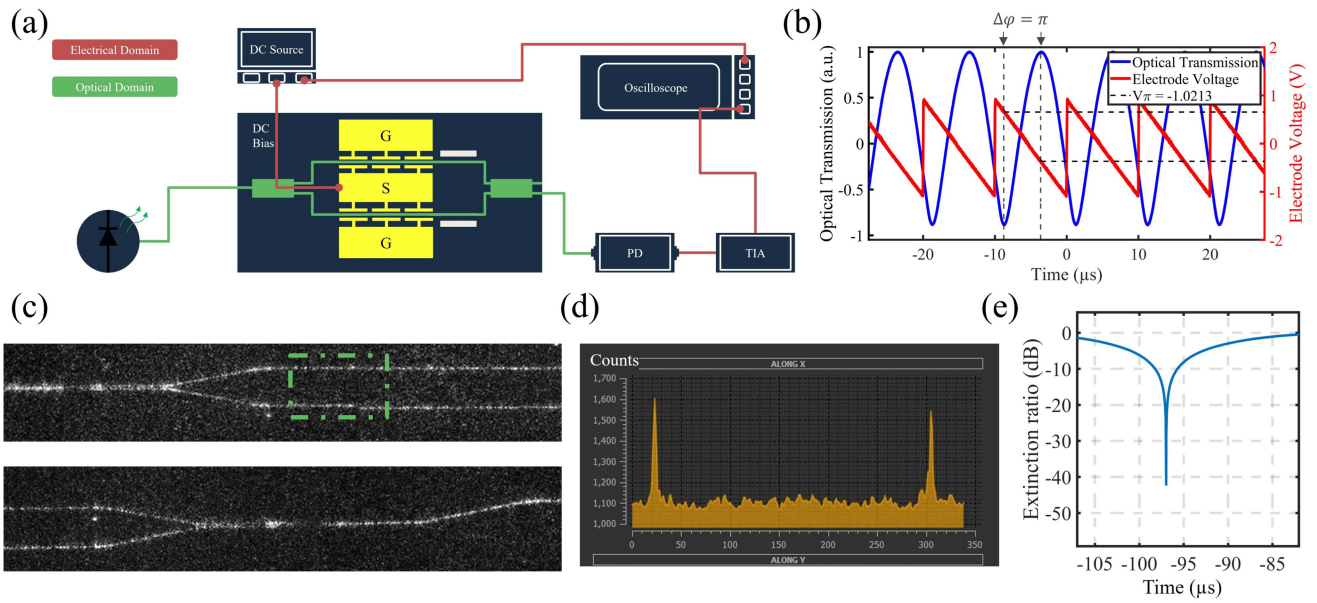


Fig. 19. (a) Schematic of the experimental setup to characterize the dual-output MZM at DC. (b) DC V_{π} Measurement. (c) 1×2 MMI input waveguide and 2×2 MMI output waveguide under IR camera with 1550 nm laser coupled. (d) The power intensity of the output port of 1×2 MMI waveguide. (e) ER measurement.

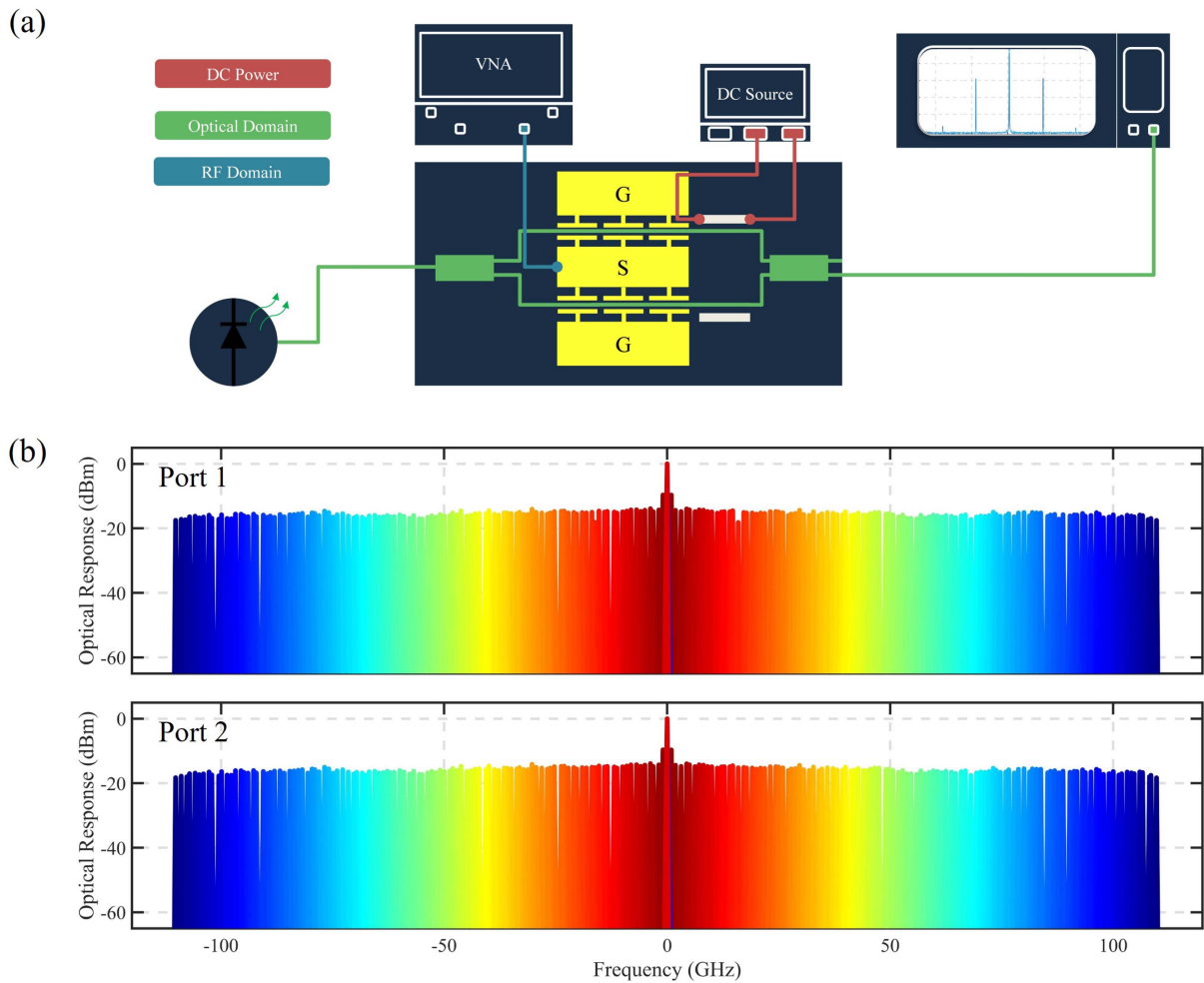


Fig. 20. (a) Schematic of the setup for high-frequency response characterization of the dual-output TFLN MZM; (b) Sideband measurement of the dual output TFLN MZM from 1 GHz to 110 GHz at near-quadrature bias.

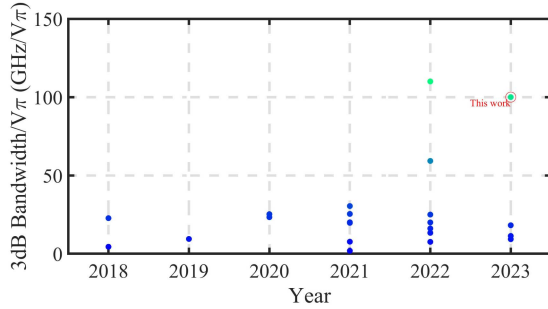
Fig. 21. Ratio of 3 dB bandwidth and V_π from 2018 to 2023.

TABLE I
TABLE OF DIFFERENT RIDGE ETCHED TFLN MODULATORS WITH MZI
PLATFORM FROM 2018 TO 2023

Year	V_π (V)	L (cm)	3 dB Bandwidth (GHz)	Reference
2018	3.8	1	20	[24]
2018	4.4	0.5	100	[25]
2018	9	0.2	40	[26]
2019	7.4	0.3	70	[27]
2020	3	0.9	70	[28]
2020	1.9	1.3	48	[29]
2021	2.74	0.5	55	[30]
2021	1.6	0.4	3	[31]
2021	3.4	0.5	67	[32]
2021	6.5	0.6	50	[33]
2021	2.36	1.3	60	[34]
2021	2.2	1	67	[35]
2022	2.8	1	70	[36]
2022	3.3	0.33	25	[37]
2022	2.7	0.6	160	[38]
2022	3.1	2	50	[39]
2022	2	1.2	40	[40]
2022	3.1	0.7	50	[41]
2022	1	2.4	110	[19]
2023	3	0.4	40	[42]
2023	2.2	0.84	40	[43]
2023	4.3	0.3	40	[44]
2023	3.52	0.4	40	[45]
2023	1.02	2	95	This Work

patterned using EBL with LOR5A and AR6200 bilayer lift-off process [15]. A 150 nm thick TiW positive metal marker was then deposited by using DC sputtering with Ti: W (10:90) target at 5 Å/s deposition rate. After liftoff the photoresist and clean the sample, 100 nm Cr film was deposited using DC sputtering with 0.5 Å/s deposition rate. ARN-7520.073 was spun at 2000 RPM and baked at 90 C for 1 min for E-beam lithography. Tracer software was used to simulate the profile of the E-beam by accounting all material stacks. BEAMER was then used to run the proximity effect correction (PEC) and apply the multi-pass function, the same waveguide pattern was written 4 times with 4 times lower dose to smooth the edge roughness. 240 $\mu\text{J}/\text{cm}^2$ and 25 nA current were used to expose the pattern. The sample was then developed using diluted AR300-47 (AR300-47: H₂O) (4:1) for 60 seconds. After development, RIE-ICP was used to etch the Cr hard mask with gas chemistry of Cl and O₂. The lithium niobate ridge was etched by applying high bias with nitrogen gas mixed with a small amount of oxygen and CF₄ for physical etching and no redeposition, as shown in Fig. 15(b). The photoresist and Cr layer were then removed by a wet etch process. A 200 nm Plasma-enhanced chemical vapor deposition

(PECVD) SiO₂ was cladded for protection and to reduce metal absorption. The thermo-optic phase shifter was written by EBL with a 50 nm step size aligned with the TiW positive alignment marker and followed by the same lift-off process. Since the undercut of LOR5A is heavy based on a bake time and temperature, the baking time of the LOR5A was increased to 20 minutes to reduce the undercut.

For segmented electrodes, AR-PC 5090.02 was spun at 4000 RPM and baked at 90 C for 1 min above the bi-layer photoresist to avoid the charging effect of EBL, since the Qz handle is not conductive. As shown in Fig. 15(c), a 1 μm gold layer was deposited using a dual-beam evaporator with a rate of 5 Å/s and 10 nm of Ti with a rate of 4 Å/s. As shown in Fig. 15(d), the sample was then diced and polished for edge coupling device characterization.

V. CHARACTERIZATION

A. Optical Loss Characterization

After the device was fabricated, the passive optical waveguide was first characterized by measuring the propagation loss. For the ridge-etched TFLN on Qz waveguide, the cutback method is not particularly expeditious due to the considerable hardness of the Qz material itself, making for time-consuming and inconsistent polishing of a smooth facet. Using Optical Backscatter Reflector (OBR) to characterize the waveguide loss is a good approach [10] to directly measure waveguide loss, but it can be challenging to ensure accuracy when the loss is below 1 dB/cm. For these reasons, the Micro-ring Resonator (MRR) technique was used to calculate the waveguide loss. In this approach, the radius of the ring was designed to be 400 μm to mitigate the bending loss caused by the mode mismatch induced by bending [16]. The gap between the ring and the waveguide was intentionally set at 400 nm to achieve critical coupling. The grating coupler (GC) was designed for light coupling, with the primary role of testing. The loss of the GC itself is of secondary concern. A continuous wave laser (CWL) was swept across the wavelength range from 1545 to 1560 nm with a step size of 0.001 nm to capture the transmission of the MMR. The omission of a data point from the peak could significantly reduce the quality factor (Q), thereby resulting in a miscalculation of the waveguide loss. The peak signal that occurred around 1550 nm was selected and fitted with a Lorentz model [17], [18]. The Full-Width at Half-Maximum (FWHM) was subsequently extracted based on this model. As a result, an intrinsic Q factors of 5.54×10^5 and a waveguide loss of 0.74 dB/cm were calculated.

B. Electrode S-Parameter Characterization

The S-parameter was characterized by using Keysight VNA with a millimeter wave frequency extender. Two GSG probes from GGB have been used to test the S-parameter of the segmented electrodes. The probes and 1 mm cable were calibrated using the smart cal OSLT (open, short, load, and through) process with the calibration kit. S₂₁ and S₁₁ were collected, as shown in Fig. 16. With the index-matched electrode, the 6 dB line indicates the estimated 3 dB bandwidth of electro-optical

modulation is around 95 GHz with an impedance of 48Ω based on the S-parameter, which provides a match with -20 dB of return loss. The RF loss was normalized to the effective length of 20 mm and plotted on the scale of the square root of the frequency. As shown in Fig. 17, a linear fit also plotted the electrode loss under 80 GHz was linear and showed a loss of $0.24 \text{ dB}/(\text{cm}\cdot\text{GHz}^{1/2})$, which shows comparable low loss from literature [7], [19].

The RF phase index was then calculated based on the measured S-parameter, and the experimental result align well with the simulation results. As shown in Fig. 18, the RF phase index matches the simulated optical group index in the second decimal place and differs by 0.002 from the simulated optical group index under 80 GHz and only 0.01 off at 110 GHz, which still provides excellent phase matching at 110 GHz. Because of the equipment limitations, measurement over 110 GHz was not possible.

C. DC Response and ER Characterization

As shown in Fig. 19(a), The DC response of the dual output modulator characterization was performed. The tunable CWL with TE-polarization was coupled into the device via edge coupling using a lensed fiber [20] with a spot diameter of $2.5 \mu\text{m}$. The coupling loss observed is attributed to the uneven edge profile and optical mode mismatch, resulting in a loss exceeding 10 dB on each facet. Consequently, an investigation of methods to reduce this coupling loss is warranted for future research. The existing literature has shown that coupling loss can be reduced by using a dual-layer inverse taper design [21] or photonic wire bonding [22]. Under the infrared camera (IR) camera, two MMI ports were selected and all scattering inside the dash green box, as shown in Fig. 19(c) was plotted in the x and y directions in a linear scale, as illustrated in Fig. 19(d). The light was then split by 1×2 MMI with a power split ratio of 50.4%:49.6%. Remarkably, the 1×2 MMI exhibited only a 0.8% difference in power splitting. The same approach has been used to monitor the power splitting ratio of the 2×2 MMI out-port. This method delivers high precision of the MMI power splitting ratio due to the selected region being only $100 \mu\text{m}$ from the MMI region and the integrated couple μm range of scattering. The output signal was coupled with lensed fiber and connected to the InGaAs photodetector. The optical signal is then converted into voltage by a trans-impedance amplifier (TIA) and monitored by an oscilloscope. The function generator was used to generate a ramp driving signal with peak-to-peak voltage (V_{pp}) of 1 V and frequency of 100 KHz. The function generator was triggered with the oscilloscope. Illustrated in Fig. 19(b), DC V_{π} of 1.02 V was measured. At peak and null bias, optical transmission was represented on a logarithmic dB scale, and more than 40 dB of ER was measured, as shown in Fig. 19(e). Notably, single-output MZM typically exhibits a lower ER, primarily due to the unwanted substrate mode coupling into output fiber as the phase swept from null to peak. In contrast, 2×2 MMI as a combiner will force the output power couple into the other port under null bias condition. Dual-output MZM with a SiN/LN platforms have been demonstrated with similar concepts as in our previous research [23].

D. High Frequency Response

The electro-optic response of the dual-output MZM was measured using the setup shown in Fig. 20(a). The 1550 nm TE-polarized CWL was coupled into the device with a 0 dBm RF signal from Keysight VNA applied on the electrode through a GSG probe. The DC source was launched on the NiCr heater to bias the device at the quadrature phase. The output of the device was coupled with a lensed fiber and connected to an optical spectrum analyzer (OSA). The RF signal on the electrode was swept from 1 GHz to 110 GHz with 1 GHz increment, and the up-converted sideband was collected for each frequency. All sideband measurements were plotted and normalized to the carrier to avoid the drift of peaks caused by the unstable coupling. The cable loss from 1 GHz to 110 GHz was collected using the Keysight RF power meter. The loss of the PICOPROBE MODEL 110H probe along with the cable loss has been factored into the optical response plot. The ultra-flat roll-off from 1 GHz to 110 GHz shown in Fig. 20(b) exhibits good phase matching for the optical waveguide and RF electrode for both ports. The peak at low frequency was due to the unterminated electrode. The 3 dB bandwidth of this device reaches up to 95 GHz, as the S_{21} measurement predicted.

As shown in Table I, all ridge-etched TFLN modulators with the MZI platform from 2018 to the most recent experimentally demonstrated work have been summarized for comparison. Due to the trade-off relationship between V_{π} and the 3 dB bandwidth, the ratio between V_{π} and the 3 dB bandwidth represents the performance of the device, as shown in Fig. 21. This device shows improved performance in comparison to other ridge-etched MZMs in the literature. And, it should be emphasized that this device is a dual-output TFLN-MZM with over 40 dB ER. In comparison to commercially available high extinction MZM (such as iXblue), the presented device also has an extended 3 dB bandwidth as well as a reduced drive voltage.

VI. CONCLUSION

In conclusion, this paper has experimentally demonstrated a TFLN-MZM with 1.02 V of V_{π} , over 40 dB ER, 48Ω impedance match, $0.24 \text{ dB}/(\text{cm}\cdot\text{GHz}^{1/2})$ electrode loss and 3 dB bandwidth around 95 GHz. The demonstration of this high-performance dual-output TFLN-MZM opens the window for broadband balanced MPLs for emerging 5 G/6 G applications.

ACKNOWLEDGMENT

The authors would like to acknowledge the significant in-kind support provided by the staff of Phase Sensitive Innovation (PSI), Inc. and the University of Delaware Nanofabrication Facility (UDNF).

REFERENCES

- [1] M. Sung et al., "Photonic THz communications based on radio-over-fiber technology for 6G mobile network: Design and opportunity," *IEEE J. Sel. Topics Quantum Electron.*, vol. 29, no. 5, pp. 1–11, Sep./Oct. 2023. [Online]. Available: <https://ieeexplore.ieee.org/abstract/document/10232877/authors#authors>
- [2] P. Yao et al., "A shot noise limited balanced microwave photonic link using an LNOI modulator and an MUTC BPD," in *Proc. IEEE Res. Appl. Photon. Defense Conf.*, 2023, pp. 1–2. [Online]. Available: <https://ieeexplore.ieee.org/abstract/document/10264709>

- [3] A. N. R. Ahmed et al., "Subvolt electro-optical modulator on thin-film lithium niobate and silicon nitride hybrid platform," *Opt. Lett.*, vol. 45, no. 5, pp. 1112–1115, 2020. [Online]. Available: <https://opg.optica.org/ol/abstract.cfm?uri=ol-45-5-1112>
- [4] X. Xie et al., "Photonic generation of high-power pulsed microwave signals," *J. Lightw. Technol.*, vol. 33, no. 18, pp. 3808–3814, Sep. 2015. [Online]. Available: <https://ieeexplore.ieee.org/document/7134695/>
- [5] X. Xiao et al., "High-speed, low-loss silicon Mach–Zehnder modulators with doping optimization," *Opt. Exp.*, vol. 21, no. 4, pp. 4116–4125, 2013. [Online]. Available: <https://opg.optica.org/oe/abstract.cfm?uri=oe-21-4-4116>
- [6] H. Yasaka et al., "High-speed InP-based Mach–Zehnder modulators for telecom applications," in *Proc. IEEE Compound Semicond. Integr. Circuit Symp.*, 2005, pp. 25–28. [Online]. Available: <https://ieeexplore.ieee.org/abstract/document/1531745>
- [7] P. Kharel, C. Reimer, K. Luke, L. He, and M. Zhang, "Breaking voltage–bandwidth limits in integrated lithium niobate modulators using microstructured electrodes," *Optica*, vol. 8, no. 3, pp. 357–363, 2021. [Online]. Available: <https://opg.optica.org/optica/abstract.cfm?uri=optica-8-3-357>
- [8] S. J. Spector et al., "CMOS-compatible dual-output silicon modulator for analog signal processing," *Opt. Exp.*, vol. 16, no. 15, pp. 11027–11031, 2008. [Online]. Available: <https://opg.optica.org/oe/abstract.cfm?uri=oe-16-15-11027>
- [9] N. Kikuchi, E. Yamada, Y. Shibata, and H. Ishii, "High-speed InP-based Mach–Zehnder modulator for advanced modulation formats," in *Proc. IEEE Compound Semicond. Integr. Circuit Symp.*, 2012, pp. 1–4. [Online]. Available: <https://ieeexplore.ieee.org/abstract/document/6340090>
- [10] X. Zhu et al., "Phase modulation using a titanium dioxide strip on lithium niobate," *Opt. Mater. Express*, vol. 12, no. 8, pp. 3296–3302, 2022. [Online]. Available: <https://opg.optica.org/ome/abstract.cfm?uri=ome-12-8-3296>
- [11] X. Huang et al., "40GHz high-efficiency Michelson interferometer modulator on a silicon-rich nitride and thin-film lithium niobate hybrid platform," *Opt. Lett.*, vol. 46, no. 12, pp. 2811–2814, 2021. [Online]. Available: <https://opg.optica.org/ol/abstract.cfm?uri=ol-46-12-2811>
- [12] J. Shin, S. R. Sakamoto, and N. Dagli, "Conductor loss of capacitively loaded slow wave electrodes for high-speed photonic devices," *J. Lightw. Technol.*, vol. 29, no. 1, pp. 48–52, Jan. 2011.
- [13] S. P. Nelan et al., "Integrated lithium niobate intensity modulator on a silicon handle with slow-wave electrodes," *IEEE Photon. Technol. Lett.*, vol. 34, no. 18, pp. 981–984, Sep. 2022.
- [14] X. Liu et al., "Sub-terahertz bandwidth capacitively-loaded thin-film lithium niobate electro-optic modulators based on an undercut structure," *Opt. Exp.*, vol. 29, no. 25, pp. 41798–41807, 2021. [Online]. Available: <https://opg.optica.org/oe/abstract.cfm?uri=oe-29-25-41798>
- [15] X. Zhu, A. J. Mercante, S. Shi, Y. Peng, and D. W. Prather, "Low loss titanium dioxide strip loaded waveguide on thin-film lithium niobate at 1550nm," in *Proc. Opt. Compon. Mater. XIX*, 2022, pp. 23–28. [Online]. Available: <https://www.spiedigitallibrary.org/conference-proceedings-of-spie/11997/1199705/Low-loss-titanium-dioxide-strip-loaded-waveguide-on-thin-film/10.1117/12.2614601.full>
- [16] P. Girault et al., "Influence of losses, device size, and mode confinement on integrated micro-ring resonator performance for absorption spectroscopy using evanescent field sensing," *J. Lightw. Technol.*, vol. 41, no. 5, pp. 1571–1581, Mar. 2023. [Online]. Available: <https://ieeexplore.ieee.org/abstract/document/9944880>
- [17] A. N. R. Ahmed, S. Shi, M. Zablocki, P. Yao, and D. W. Prather, "Tunable hybrid silicon nitride and thin-film lithium niobate electro-optic microresonator," *Opt. Lett.*, vol. 44, no. 3, pp. 618–621, 2019. [Online]. Available: <https://opg.optica.org/ol/abstract.cfm?uri=ol-44-3-618>
- [18] L.-W. Luo, G. S. Wiederhecker, J. Cardenas, C. Poitras, and M. Lipson, "High quality factor etchless silicon photonic ring resonators," *Opt. Exp.*, vol. 19, no. 7, pp. 6284–6289, 2011. [Online]. Available: <https://opg.optica.org/oe/abstract.cfm?uri=oe-19-7-6284>
- [19] M. Xu et al., "Dual-polarization thin-film lithium niobate in-phase quadrature modulators for terabit-per-second transmission," *Optica*, vol. 9, no. 1, pp. 61–62, 2022. [Online]. Available: <https://opg.optica.org/optica/abstract.cfm?uri=optica-9-1-61>
- [20] "Tpmj-3a-1550-8125-025-7-25-14-2," [Online]. Available: <https://shop.ozoptics.com/tpmj-3a-1550-8125-025-7-25-14-2>
- [21] L. He et al., "Low-loss fiber-to-chip interface for lithium niobate photonic integrated circuits," *Opt. Lett.*, vol. 44, no. 9, pp. 2314–2317, 2019. [Online]. Available: <https://opg.optica.org/ol/abstract.cfm?uri=ol-44-9-2314>
- [22] V. Rosborough et al., "Photonic wire bonding via two-photon polymerization laser lithography for hybrid integration," in *Proc. Integr. Opt., Devices, Mater., Technol. XXVII*, 2023, pp. 147–151. [Online]. Available: <https://www.spiedigitallibrary.org/conference-proceedings-of-spie/12424/124240Q/Photonic-wire-bonding-via-two-photon-polymerization-laser-lithography-for/10.1117/12.2647641.full>
- [23] S. P. Nelan et al., "Ultra-high extinction dual-output thin-film lithium niobate intensity modulator," *IEEE Access*, vol. 10, pp. 100300–100311, 2022. [Online]. Available: <https://ieeexplore.ieee.org/document/9895241>
- [24] A. J. Mercante et al., "Thin film lithium niobate electro-optic modulator with terahertz operating bandwidth," *Opt. Exp.*, vol. 26, no. 11, pp. 14810–14816, 2018. [Online]. Available: <https://opg.optica.org/oe/abstract.cfm?uri=oe-26-11-14810>
- [25] C. Wang et al., "Integrated lithium niobate electro-optic modulators operating at CMOS-compatible voltages," *Nature*, vol. 562, no. 7725, pp. 101–104, 2018. [Online]. Available: <https://www.nature.com/articles/s41586-018-0551-y>
- [26] C. Wang, M. Zhang, B. Stern, M. Lipson, and M. Lončar, "Nanophotonic lithium niobate electro-optic modulators," *Opt. Exp.*, vol. 26, no. 2, pp. 1547–1555, 2018. [Online]. Available: <https://opg.optica.org/oe/abstract.cfm?uri=oe-26-2-1547>
- [27] M. He et al., "High-performance hybrid silicon and lithium niobate Mach–Zehnder modulators for 100 gbit/s and beyond," *Nature Photon.*, vol. 13, no. 5, pp. 359–364, 2019. [Online]. Available: <https://www.nature.com/articles/s41566-019-0378-6>
- [28] S. Sun et al., "Bias-drift-free Mach–Zehnder modulators based on a heterogeneous silicon and lithium niobate platform," *Photon. Res.*, vol. 8, no. 12, pp. 1958–1963, 2020. [Online]. Available: <https://opg.optica.org/prj/abstract.cfm?uri=prj-8-12-1958>
- [29] M. Xu et al., "High-performance coherent optical modulators based on thin-film lithium niobate platform," *Nature Commun.*, vol. 11, no. 1, 2020, Art. no. 3911. [Online]. Available: <https://www.nature.com/articles/s41467-020-17806-0>
- [30] J. Hu et al., "Folded thin-film lithium niobate modulator based on a poled Mach–Zehnder interferometer structure," *Opt. Lett.*, vol. 46, no. 12, pp. 2940–2943, 2021. [Online]. Available: <https://opg.optica.org/ol/abstract.cfm?uri=ol-46-12-2940>
- [31] M. Jin, J. Chen, Y. Sua, P. Kumar, and Y. Huang, "Efficient electro-optical modulation on thin-film lithium niobate," *Opt. Lett.*, vol. 46, no. 8, pp. 1884–1887, 2021. [Online]. Available: <https://opg.optica.org/ol/abstract.cfm?uri=ol-46-8-1884>
- [32] X. Liu et al., "Wideband thin-film lithium niobate modulator with low half-wave-voltage length product," *Chin. Opt. Lett.*, vol. 19, no. 6, 2021, Art. no. 0 60016. [Online]. Available: <https://opg.optica.org/col/abstract.cfm?uri=col-19-6-060016>
- [33] J. Rollinson, M. Hella, S. Toroghi, P. Rabiei, and I. Wilke, "Thin-film lithium niobate modulators for non-invasive sensing of high-frequency electric fields," *J. Opt. Soc. Amer. B*, vol. 38, no. 2, pp. 336–341, 2021. [Online]. Available: <https://opg.optica.org/josab/abstract.cfm?uri=josab-38-2-336>
- [34] P. Ying et al., "Low-loss edge-coupling thin-film lithium niobate modulator with an efficient phase shifter," *Opt. Lett.*, vol. 46, no. 6, pp. 1478–1481, 2021. [Online]. Available: <https://opg.optica.org/ol/abstract.cfm?uri=ol-46-6-1478>
- [35] G. Chen et al., "High performance thin-film lithium niobate modulator on a silicon substrate using periodic capacitively loaded traveling-wave electrode," *APL Photon.*, vol. 7, no. 2, 2022, Art. no. 026103. [Online]. Available: <https://doi.org/10.1063/5.0077232>
- [36] X. Huang et al., "Linearity-enhanced dual-parallel Mach–Zehnder modulators based on a thin-film lithium niobate platform," vol. 9, no. 3, 2022, Art. no. 197. [Online]. Available: <https://www.mdpi.com/2304-6732/9/3/197>
- [37] C. Li et al., "High modulation efficiency and large bandwidth thin-film lithium niobate modulator for visible light," *Opt. Exp.*, vol. 30, no. 20, pp. 36394–36402, 2022. [Online]. Available: <https://opg.optica.org/oe/abstract.cfm?uri=oe-30-20-36394>
- [38] X. Liu et al., "Capacitively-loaded thin-film lithium niobate modulator with ultra-flat frequency response," *IEEE Photon. Technol. Lett.*, vol. 34, no. 16, pp. 854–857, Aug. 2022. [Online]. Available: <https://ieeexplore.ieee.org/document/9782315/>
- [39] Y. Pan et al., "Compact substrate-removed thin-film lithium niobate electro-optic modulator featuring polarization-insensitive operation," *Opt. Lett.*, vol. 47, no. 7, pp. 1818–1821, 2022. [Online]. Available: <https://opg.optica.org/ol/abstract.cfm?uri=ol-47-7-1818>

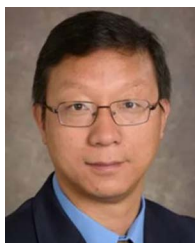
- [40] M. Wang et al., "Thin-film lithium-niobate modulator with a combined passive bias and thermo-optic bias," *Opt. Exp.*, vol. 30, no. 22, pp. 39706–39715, 2022. [Online]. Available: <https://opg.optica.org/oe/abstract.cfm?uri=oe-30-22-39706>
- [41] R. Wu et al., "High-production-rate fabrication of low-loss lithium niobate electro-optic modulators using photolithography assisted chemo-mechanical etching (PLACE)," *Micromachines*, vol. 13, no. 3, 2022, Art. no. 378. [Online]. Available: <https://www.mdpi.com/2072-666X/13/3/378>
- [42] N. Chen, Y. Yu, K. Lou, Q. Mi, and T. Chu, "High-efficiency thin-film lithium niobate modulator with highly confined optical modes," *Opt. Lett.*, vol. 48, no. 7, pp. 1602–1605, 2023. [Online]. Available: <https://opg.optica.org/ol/abstract.cfm?uri=ol-48-7-1602>
- [43] H. Li et al., "Compact thin-film lithium niobate modulators using slotted coplanar waveguide electrode suitable for high-volume fabrication," *J. Phys. D, Appl. Phys.*, vol. 56, no. 15, 2023, Art. no. 154001. [Online]. Available: <https://dx.doi.org/10.1088/1361-6463/acbb13>
- [44] Y. Li et al., "High-performance Mach-Zehnder modulator based on thin-film lithium niobate with low voltage-length product," *ACS Omega*, vol. 8, no. 10, pp. 9644–9651, 2023. [Online]. Available: <https://doi.org/10.1021/acsomega.3c00310>
- [45] N. Chen, K. Lou, Y. Yu, X. He, and T. Chu, "High-efficiency electro-optic modulator on thin-film lithium niobate with high-permittivity cladding," 2023, *arXiv:2304.06946*.



Xiaofeng Zhu received the B.S. degree in chemistry, in 2020 from the University of Delaware, Newark, DE, USA, where he is currently working toward the Ph.D. degree with the Department of Electrical and Computer Engineering. His research interests include lithium niobate on insulator photonics and Microwave photonic links.



Marco Moller de Freitas received the B.S. degree in telecommunications engineering from FUMEC University, Belo Horizonte, Brazil, in 2009. He is currently working toward the Ph.D. degree with concentration in electromagnetics and photonics with the University of Delaware, Newark, DE, USA. After more than a decade working in the telecommunications industry, he started his Ph.D. degree. His research interests include RF photonics, millimetric wave antennas, and radio frequency over fiber (RFoF).



Shouyuan Shi (Member, IEEE) received the B.S., M.S., and Ph.D. degrees in electrical engineering from Xidian University, Xi'an, China, in 1991, 1994, and 1997, respectively. He is currently a Research Professor with the Department of Electrical and Computer Engineering, University of Delaware, Newark, DE, USA. He is also a Consulting Engineer with Phase Sensitive Innovations, Inc., Newark, DE. He has authored or coauthored eight books and book chapters, and more than 380 peer refereed journal and conference publications. He holds more than 20 issued U.S. patents. His research interests include computational electromagnetics, micro-optics and nano-photonics, and RF-photonics technologies and applications, including ultra-wideband RF antennas, optically addressed phase arrays, ultra-wideband electro-optic devices and systems, passive and active millimeter wave imaging systems. He is also an active Reviewer of more than 20 international peer-reviewed journals in the research areas of optics and photonics, RF, electro-optics, and electromagnetics. He was the Topic Editor of Photonic Devices and Materials, *Optical and Photonic Letters*, and the Editorial Board Member of *Advanced Optics*.



Andrew Mercante received the B.S. degree in electrical engineering from the University of Delaware, Newark, DE, USA, in 2013, and the Ph.D. degree, in 2018. He is currently conducting a Postdoctoral Research with Phase Sensitive Innovations Inc., where his research interests include further development of thin-film lithium niobate devices and heterogeneous integration of materials. His focus is on the design and fabrication of ultra-wideband electro-optic phase modulators in thin-film lithium niobate.



Peng Yao received the B.S. and M.S. degrees from the Department of Mechanical Engineering, Xi'an Jiaotong University, Xi'an, China, in 1998 and 2001, respectively, and the Ph.D. degree in nano and micro fabrication of electronic and optical devices from the Graduate School, University of Delaware, Newark, DE, USA, in 2007. In 2007, he joined Phase Sensitive Innovations, as the Lead Engineer in new component Research and Development and is responsible for the development of the world leading LN modulator products and high-power photodiode products. He has authored or coauthored one book chapter and more than 50 peer reviewed journals and international conference papers. He holds two issued U.S. patents and seven provisional patents. His research interests include broadband LN or LNOI modulators, high-speed and high power photodiodes, packaging of high frequency passive and active components, microwave photonic links, micro fabrication techniques, and passive and active millimeter wave imaging systems.



Fuquan Wang received the B.S. and M.S. degrees in electrical engineering from Chongqing University, Chongqing, China, in 2009 and 2012, respectively. He is currently working toward the doctoral degree as a Research Assistant with the Department of Electrical and Computer Engineering, University of Delaware, Newark, DE, USA. His research interests include microwave and millimeter-wave antenna design, RF photonics phased array transmitter and receiver, signal linearity optimization on optical modulators, and high-speed high-power photodiodes.



Benjamin A. Shopp received the bachelor's degree in electrical engineering from the University of Delaware, Newark, DE, USA, in 2020. After completing his bachelor's degree, he has been conducting research with Phase Sensitive Innovations Inc., focusing on optical testing/integration, development, and fabrication of thin-film lithium niobate devices.



modulation, and thin-film lithium niobate.

Christopher J. Cullen received the B.S. degree in electrical and computer engineering from Rowan University, Glassboro, NJ, USA, in 2014, and the M.S. degree in electrical engineering, in 2018 from the University of Delaware, Newark, DE, USA, where he is currently working toward the Ph.D. degree. He is also the Chemical Hygiene Office and Fabrication Engineer with Phase Sensitive Innovations Inc. based in Newark, DE, USA, where he started as an employee in 2018. His research interests include micro- and nano-fabrication techniques, electro-optic



In 1997, he joined the Department of Electrical and Computer Engineering, University of Delaware, Newark, DE, USA, where he is currently the College of Engineering Alumni Distinguished Professor. His research interests include theoretical and experimental aspects of RF-phonic elements and their integration into various systems for imaging, communications, and Radar. Dr. Prather is an Endowed Professor of electrical engineering, Fellow of National Academy of Inventors, Fellow of the Society of Photo-Instrumentation Engineers, and Fellow of the Optica formerly Optical Society of America.

Dennis W. Prather (Fellow, IEEE) received the B.S.E.E., M.S.E.E., and Ph.D. degrees from the University of Maryland, College Park, MD, USA, in 1989, 1993, and 1997, respectively, after serving three years of active duty. He began his professional career by joining the U.S. Navy in 1982 as an E-1, where he served until 2021 and retired at the rank of CAPT (O-6) as an Engineering Duty Officer. He was a Senior Research Engineer with the Army Research Laboratory, where he performed research on both optical devices and architectures for information processing.